Bioimpedance-based investigation of anti-oxidant nanotherapeutics against intracellular oxidative stress

Gaurav Pandey[1,2,] Murugan Veerapandian[1,2]*

[1]*Electrodics and Electrocatalysis Division, CSIR-Central Electrochemical Research Institute, Karaikudi 630 003, Tamil Nadu*

[2]*Academy of Scientific & Innovative Research (AcSIR), Ghaziabad 201 002, India*

**Corresponding Author: vmurugan@cecri.res.in*

Abstract:

This study presents a non-invasive bioimpedance-based investigation using an electric cell-substrate impedance sensing system (ECIS) to evaluate the pharmacological effects of molybdenum trioxide hybridized Kaempferol nanoparticles (MoHK NPs) against intracellular oxidative stress. Employing gold-microelectrode array wells, we monitored the real-time responses of RAW 264.7 cells to various physical and chemical oxidative stress stimuli. The ECIS-derived biophysical parameters, including impedance, resistance, and capacitance, demonstrated the anti-oxidant properties of MoHK NPs, corroborated by conventional assays. This comprehensive spatial assessment provides a valuable framework for similar cellomics studies.

Keywords: *oxidative stress; cell-nanomaterial interface; ECIS; nanomedicine; semi-synthetic anti-oxidants*

1.Introduction

Cellular oxidative stress is a primary cause of chronic inflammation [1]. Therefore, there is an increasing need to understand the pathophysiology of cellular oxidative stress and develop preventative medication [1–3]. The cells under persistent radical oxygen species (ROS) attack predominate pathophysiological conditions, escalating oxidative stress [4,5]. Further, it activates various transcription factors, which cause the expression of respective genes associated with inflammatory pathways [6,7]. Hence, cells need anti-oxidant to control ROS under severe stress, either by catalysis or through a radical scavenging mechanism [5]. With the advent of cellular oxidative stress, anti-oxidants garnered significant interest as a health supplements. Dietary polyphenols contribute various biological function, including prevention of oxidative stress and degenerative illnesses. They are regarded as effective ROS scavengers because of its aromaticity and hydroxyl groups in a highly conjugated system, they can prevent oxidative damage to biomolecules (lipids, proteins, and DNA) by suppressing cellular oxidative stress and reducing tissue inflammation. Pre-clinical studies show that the long-term consumption of high polyphenol diets offers protection against the emergence of various chronic diseases, including cancer, cardiovascular, diabetes, infectious, and neurodegenerative diseases [6]. However, polyphenols suffer with standardization and bioavailability. For instance, polyphenols may reach the colon because of their insufficient absorption, where they are digested by the gastrointestinal tract (GIT) microbiota and produce several bacterial metabolites. Hence, it can be potentially toxic during prolonged use [8]. Therefore, increasing the bioavailability through different tools such as a prodrug, linker chemistry, bypassing GIT, and size reduction is of prime importance. Nanotherapeutics is a growing novel drug discovery field with several potential advantages over traditional drugs. NPs can be designed with specific properties, such as surface charge, hydrophobicity, and biocompatibility, to enhance interaction with biological systems [9]. The NP-based delivery system has shown improved pharmacokinetics compared to traditional drugs, resulting in increased bioavailability, site-specific delivery, enhanced therapeutic efficacy, reduced toxicity, and stability. The ability to manipulate and use the properties of NPs for targeted delivery has made

nanotherapeutics a rapidly growing area of research and development in drug discovery [10]. Utilizing nano-chemistry, herein, hydrophobic polyphenol, *i.e.,* kaempferol, is hybridized with molybdenum trioxide (MoO_3) NPs to form molybdenum tri-oxide hybridized kaempferol (MoHK) NPs. MoO_3 stands out among transition metal oxides (TMOs) due to its versatile properties and wide range of applications [11,12]. Unlike many other TMOs, MoO_3 can exist in various stoichiometries, with intermediate phases that exhibit distinct biological properties [13]. This variability is crucial for applications in cellular biology. Molybdenum of MoO_x is a well-known cellular micronutrient and metal cofactor for several enzyme, metalloprotein, and possess enzyme mimicking activity [14]. Similarly, Kaempferol has been known to possess anti-oxidant and anti-inflammatory properties [15]. Moreover, the presence of conjugated π-bonds and nucleophilic sites/ steric arrangement resulting from oxygenated functional groups renders Kaempferol a favorable option for coordination with metals [16]. Kaempferol demonstrates both direct and indirect pathways to eliminate reactive oxygen species by producing anti-oxidant enzymes. Kaempferol mitigates oxidative stress by disrupting immune-metabolic and NF-κB signaling pathways [15]. MoO_3 in hybridized systems found to enhance the synergism for effective biomedical properties [16,17]. Owing to its nano chemistry and anti-oxidant activity, herein, MoO_3-hybridized Kaempferol has been chosen as model system to monitor the oxidative stress scavenging assay.

These MoHK NPs are investigated using electric cell-substrate impedance sensing (ECIS) as a potential preventive medicine against differently induced oxidative stress. ECIS provides an edge over other *in vitro* methods due to its *in situ*, *non-invasive*, and real-time monitoring characteristics *via* electrical resistance signals [18–21]. Bioimpedance methods have recently emerged as a promising technique for assessing metastasis, regenerative and personalized medicine, infections, and environmental toxicants [20–23]. Additionally, excluding conventional labeling is possible when resistance is used as a cellular readout. This can restore cells to their natural and physiologically relevant state and avoid their detrimental effects on cellular activities. In addition, the ECIS system provides kinetic data on initial cell attachment and sustained steady-state adhesion in real-time. Therefore, ECIS can discriminate biophysical cellular events like morphological changes, adhesion, proliferation, pathological condition, and response to xenobiotics. Capacitance/resistance/impedance originating from the cellular event, such as motility on or off the working electrode, can provide details with a spatial resolution of less than 1 nm. Thus, ECIS enables quantitative real-time measurement, eliminating the need for periodic frequent sample collection and tedious post-experimental processing.

Herein, the ECIS ZΘ system (Applied Biophysics, USA) with electrode array of eight wells, each containing ten gold-microelectrodes (8W10E), are utilized. ECIS modelling is performed in constant phase element (CPE) alternative to capacitor considering the non-homogeneity of the system. The ECIS system capable of recording impedance (Z), resistance (R), and capacitance (C), at the same time for multiple frequencies. Therefore, it enables a better understanding of the cells' structural and chemical dispersity. The approach works by monitoring changes in the AC impedance of tiny gold-film microelectrodes (*d*: 250 μm) utilized as a growth substrate. Compared to conventional methods, which often rely on invasive procedures and continuous monitoring, using ECIS as an alternative assay platform does not require complex experimental processing with comparable results to cell and animal models. Thus, different physical (photoirradiation and thermal exposure) and chemical (oxidative and inflammatory agents) induced oxidative

stress, and the healing function of nanotherapeutics are studied utilizing ECIS. It is envisioned that this cellular electrical impedimetric assay platform will be a valuable tool in the rapid preclinical investigation of potential anti-oxidant drug leads.

2. Materials and methods

Reagents and materials used for this work is provided in supplementary information (SI).Information on instruments used in this work is provided in SI.

MoO_3 hybridized Kaempferol nanoparticles (MoHK NPs)were synthesized based on our earlier report [24] and the synthesis procedure is provided in SI. Each ECIS chip was pre-treated with 10 mM L-cysteine for 10 min, rinsed thrice with DI water, dried, and stored for further experiments.

Cell sub-culturing and seeding on ECIS chips was carried out as follows :

Once the RAW 264.7 cell line reached approximately 90% confluency, it is selected for sub-culturing. Firstly, the culture medium is aspirated from the T-25 flask. Followed by trypsinization using trypsin-EDTA (~1.5 mL) than incubating T-25 flask at 37 °C for 5 minutes. Post incubation, the cells are detached by gently tapping the sides of flask. Fresh DMEM media is then added to the flask to neutralize the EDTA. The cell suspension is gently pipetted to ensure thorough mixing. A small aliquot of the suspended cells is subsequently transferred to a hemocytometer for cell counting. Prior to cell seeding, the ECIS chips are equilibrated with a serum-free medium inside a CO_2 incubator. Based on the cell count, the cells are transferred to the new growth media and seeded into wells of ECIS chips at a density of approximately 3 to 5 × 10^5 cells/cm^2.

UV light-induced ROS generation was carried out as follows :

For UV irradiation, the cells are transferred into Eppendorf's tube and divided into half as treated and untreated; all the aliquots are incubated for 5 h in a CO_2 incubator before UV exposure. The UV treatment was performed for 2, 5, and 10 min using a UV-C lamp (λ = 254 nm) as a source. Post-irradiated cells were then inoculated in ECIS chip containing wells for bioimpedance measurement. The cells without treatment are chosen as control and PBS as a blank (B).

For heat shock generation, an Eppendorf's tubes were loaded with RAW 264.7 cells (5 × 10^5 cells/cm^2) before heat shock treatment. Following, both sample-treated and untreated vials were cultured in a CO_2 incubator for 5 h. For inducing the heat shock, vials are kept in a hot water bath maintained at 45 °C temperature for 2, 5, and 10 min. Followed by seeding in wells of chips for ECIS analysis. Cells with no treatment acted as control.

Oxidative stress was induced using 3.5 µL of 30% H_2O_2. MoO_3, Kaempferol, and MoHK are added in 5 µg concentration. Ascorbic acid and gallic acid are used as a reference at 27.5 and 38.2 µM [25,26], respectively. DMEM medium without and with H_2O_2 treatment is taken as negative (NC) and positive control (PC), respectively.

A 5 µg of MoO_3 NPs, Kaempferol, and MoHK NPs were inoculated at 16 h in ECIS wells. After a confluent stage, PGE2 of two concentrations (10 µg and 10 ng) was added at 44 h. Similarly, a cell containing DMEM with and without PGE2 treatment was taken as an PC and NC, and PBS as blank for comparative analysis.

Conventional cellular assay was carried out for Cytocompatibility assay a 100 µL aliquot of DMEM containing approximately 5×10^4 RAW 264.7 cells/cm^2 was seeded into 96 well (flat bottom) tissue culture plates with 5, 10, and 30 µg of samples. After 24 h of incubation, 10 µL of MTT labeling reagent (0.5 mg/mL) is added to each well. Following an additional 4 h incubation with the MTT reagent, 100 µL of solubilization buffer is added to each well and incubated for 24 h. Afterward, the solubilized purple formazan crystals were measured

at λ 580 nm.

For H_2O_2 assay RAW 264.7 (5×10^4 cells/cm^2) cells were pre-incubated with test samples and standard anti-oxidants for 24 h. Followed by 100 μM of H_2O_2 was added and incubated for 1 h to determine the influence of test samples. Afterward, an assay buffer was added and kept aside for an additional hour. The intracellular H_2O_2 concentration is determined at an $\lambda_{ex}/\lambda_{em}$ of 490/520 nm.

For Anti-oxidant assay test sample treated RAW 264.7 (5×10^4 cells/cm^2) cells are pre-incubated for 4 h in black-colored polystyrene 96 well plates, followed by treatment with PGE2 (10 μg) and incubated for 24 h. 20 μL DCFDA at a concentration of 100 μM was added into each well and incubated for another 30 min. After the reagent, cells in the medium was maintained in a CO_2 incubator. The fluorescence measured at λ_{ex} of 485 and λ_{em} of 530 nm.

3. Results and Discussion

3.1 ECIS-based cyto-viability assay

Figure:1 shows the representative ECIS well-based electrode system for measuring the bioimpedance against different external stimuli. From the ECIS-cell interface the cell coverage capacitance (C; farad/ F), and cell barrier function are correlated by monitoring the electrical resistance (R/ Ω). With multifrequency ECIS modeling, changes in the capacitance at the cell membrane (C_m; μF/Ω-cm^2), intercellular resistance (R_b; Ω-cm^2), and cell-substrate basolateral adhesion (α; Ω-cm$^{1/2}$) are studied (please refer SI for more information). Due to the specific geometry of gold electrodes and the deduction of external resistive factor, the involvement of electrode capacitance (C_E) and resistance (R_E, R_{med}, and R_{sub}) to the whole circuit becomes negligible [21]. The area of the lateral cell membrane is calculated using the macrophage cellular dimension (radius: 10-20 μm, thickness: 15-30 μm). Refined estimation of the area of the lateral cell membrane accounting for the dimensions of RAW 264.7 cells in equation (S1) enabled us to find the models that best fit our data. This correlation is used to comprehend the physical characteristics of RAW 264.7 cells and its membranous activities, such as adhesion, transport, and signaling. At first, the L-cysteine pretreated ECIS 8W10E wells are subjected to frequency scan and stabilization. L-cysteine facilitates the formation of cell monolayer over the gold-microelectrode owing to binding with filopodia of cells. The cell-free capacitance of the electrode is found to be 30 ± 5 nF.

Figure 2(a) shows no resistance change in initial cell adherence. After 2 h, cells bind on the gold-microelectrode through extracellular matrix (ECM) proteins and filopodia. The cells' attachment and spreading are observed with an increased well resistance. At t = 20 h, the wells are inoculated with test samples, and no cell-substrate detachment is observed other than MoO_3 NPs. Additionally, cell micromotion is traced through oscillating resistance. Until the cell growth reaches its full confluence, asynchronous growth observed in the well-reflected with the gradual increase in resistance. The culture media are replenished at t = 40 and t = 70 h. The sample-treated wells showed faster confluent barrier formation. As observed under the sub-confluence stage, electrode resistance found proportional to the cell numbers with a sudden decrease in resistance post-sample inoculation implied cytotoxicity. Upon reaching confluency, the cell growth-associated morphological changes raised a series of peaks and valleys. The cell status is observed by tracking the resistance at different periods showing a higher resistance for MoHK for prolonged time (**Fig**. S3). The EC_{50} concentration for MoHK NPs is found from dose response curve, which is observed to be ~5 μg (**Fig**. S4). This concentration is used for further experiments

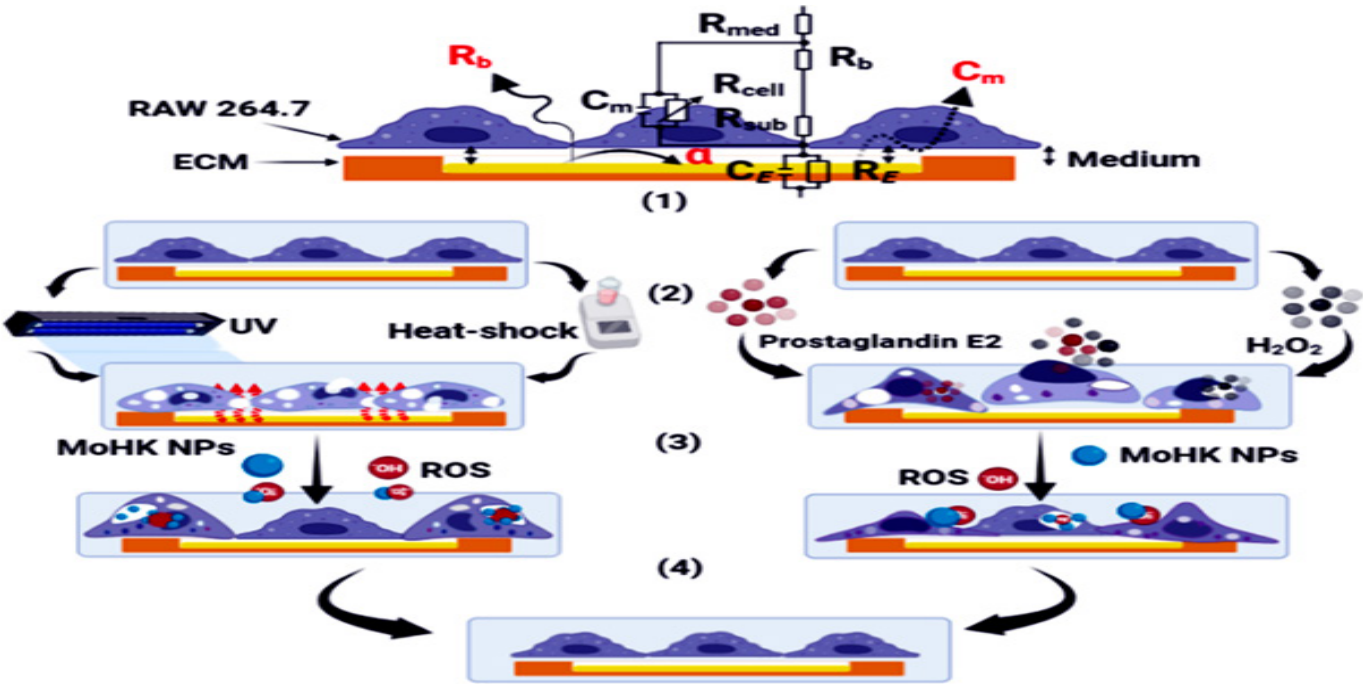


Figure 1. Illustrate the ECIS experimental workflow. ECIS gold-microelectrode chip grown RAW 264.7 cells represented with an equivalent circuit diagram showing the electrical components responsible for bioimpedance, (1) *in situ* grown cells on gold microelectrode. (2) Induction of oxidative stress *via* both physical (left panel) and chemical (right panel) to study biophysical dysfunction in cells. (3) Post-cellular oxidative stress and inoculation of MoHK as an anti-oxidant by ROS scavenging. (4) Cell healing process *via* ROS scavenging mediated by MoHK NPs.

Figure 2(a) shows no resistance change in initial cell adherence. After 2 h, cells bind on the gold-microelectrode through extracellular matrix (ECM) proteins and filopodia. The cells' attachment and spreading are observed with an increased well resistance. At t = 20 h, the wells are inoculated with test samples, and no cell-substrate detachment is observed other than MoO_3 NPs. Additionally, cell micromotion is traced through oscillating resistance. Until the cell growth reaches its full confluence, asynchronous growth observed in the well-reflected with the gradual increase in resistance. The culture media are replenished at t = 40 and t = 70 h. The sample-treated wells showed faster confluent barrier formation. As observed under the sub-confluence stage, electrode resistance found proportional to the cell numbers with a sudden decrease in resistance post-sample inoculation implied cytotoxicity. Upon reaching confluency, the cell growth-associated morphological changes raised a series of peaks and valleys. The cell status is observed by tracking the resistance at different periods showing a higher resistance for MoHK for prolonged time (**Fig**. S3). The EC_{50} concentration for MoHK NPs is found from dose response curve, which is observed to be ~5 µg (**Fig**. S4). This concentration is used for further experiments

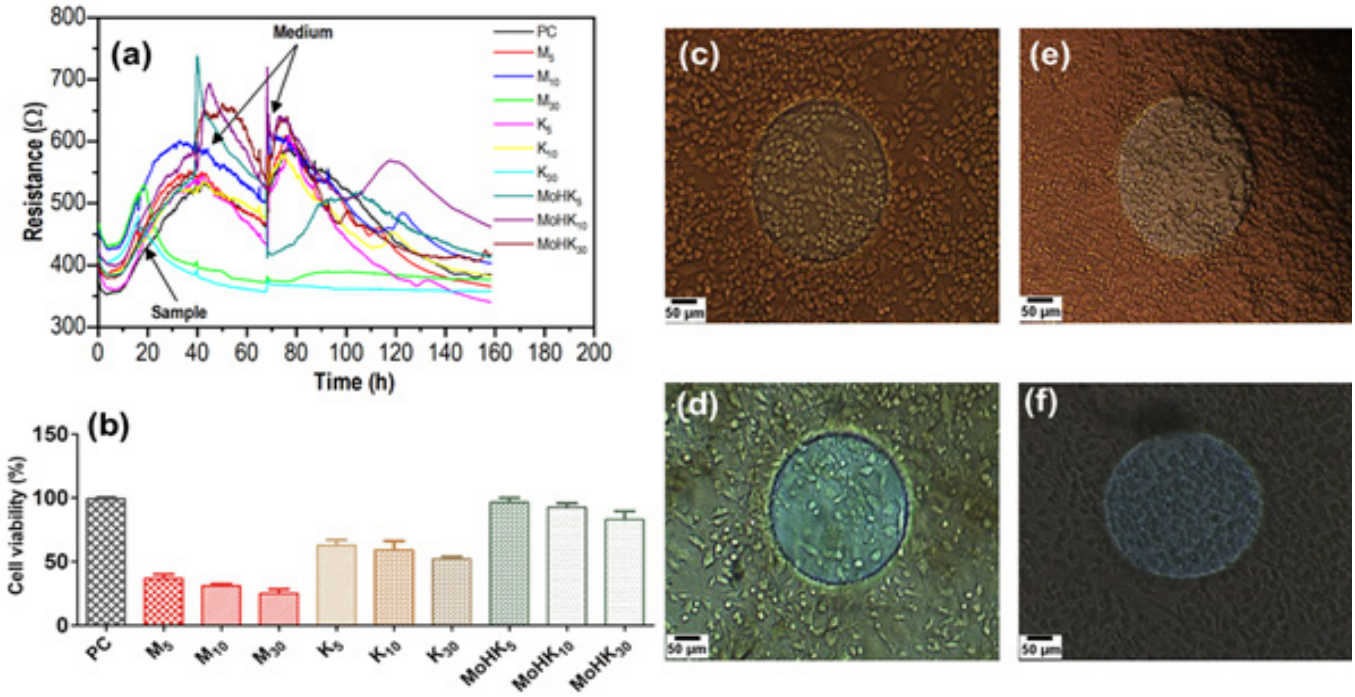


Figure 2. (a) Represents ECIS resistance *vs* time-based cells biophysical response data for all wells. (b) MTT assay with a significant difference in cytocompatibility concerning treated test sample (P<.001) determined using One-way ANOVA and optical microscope images where (c) Positive control, (d) MoO_3, (e) MoHK, and (f) Kaempferol at 20×.

Resistance data suggest that the MoHK NP treated wells formed cell monolayer efficiently compared to MoO_3 and Kaempferol, even at 30 µg. The resistance vs frequency data details the electrical characteristics of cells cultivated on the substrate. The multiple frequency analysis (**Fig**. S5) shows the concentration-effect on cell growth for test samples for range of frequencies (62.5 Hz to 64 kHz), which can be further converted to traceable capacitance and cellular capacitance. It can be observed that there has been a resistance variance for the same concentration of the different tested samples. Changes in the spreading and adhesion of cells on the substrate are reflected in the reduction of resistance with respect to frequency. The magnitude and velocity of this decline suggest a firm substrate and cell adhesion phenomenon. The time-dependent variations in resistance at various frequencies suggest the cell viability and vitality. A fall in resistance was observed with increased frequency because of a build-up in barriers across the cell due to cell growth and proliferation that prevented the passage of electrical current. **Fig**. S6 shows the modeled data for R_b (a), α (b), and C_m (c). Herein, MoHK NPs treated wells exhibit superior cell attachment, spreading/micromotion, and proliferation throughout the study as observed in the model fit providing the R_b, α, and C_m at 0.13 $\Omega.cm^2$, 1.4 $cm.\Omega^5$, and 0.001 $\mu F/cm^2$, respectively, with a minimum drift of 1.7 % and root mean squared error (RMSE) of 0.005.

Conventional MTT assay for MoHK NPs are tested using Raw 264.7 cells. The cells are seeded into 96-well plates, treated with different concentrations *viz*. 5, 10, 30 µg of MoHK NPs as well as pristine MoO_3 and kaempferol along with control (medium) and 10% FBS (fetal bovine serum) for 24 h. It can be seen that 10 µg and above concentrations of kaempferol have shown a toxic effect on cell viability, while MoO_3 and MoHK NPs at the given concentrations found to be non-toxic. MoO_3 NPs at 5 and 10 µg and MoHK NPs at concentrations 5, 10, and 30 µg have shown no adverse effect on cell viability and proliferation. Notably, both MoO_3 and MoHK NPs are found to be non-cytotoxic and did not elicit a negative response with cell viabilities for all dilutions tested (**Fig.** 2b). However, at 30 µg both pristine test samples enabled a drastic decline in the resistance, indicating a detrimental effect on the treated cell lines. This particular result is in coherence with the MTT assay results. Microscopic images taken at t = 70 h show cells attached to gold-microelectrode. Cell proliferation is observed in the order of MoHK > control > kaempferol > MoO_3. Distinctively, MoHK and kaempferol possess superior cytocompatibility at higher doses of 30 µg (**Fig**. 2 c-f). In the resistance *vs* time plot, a high concentration of MoO_3 shows cell mortality, as observed with decreased resistance response. Cells with high dosing of MoO_3 NPs caused cell death and lost the adherence character. Hence, detached from the gold microelectrode. MoHK provided superior cell viability compared to MoO_3 and kaempferol, even at a high concentration of 30 µg. This ECIS data is validated with the *in vitro* cell viability assay using MTT dye and found to be identical. The cyto-viability studies ensured the biocompatibility of the nanotherapeutics.

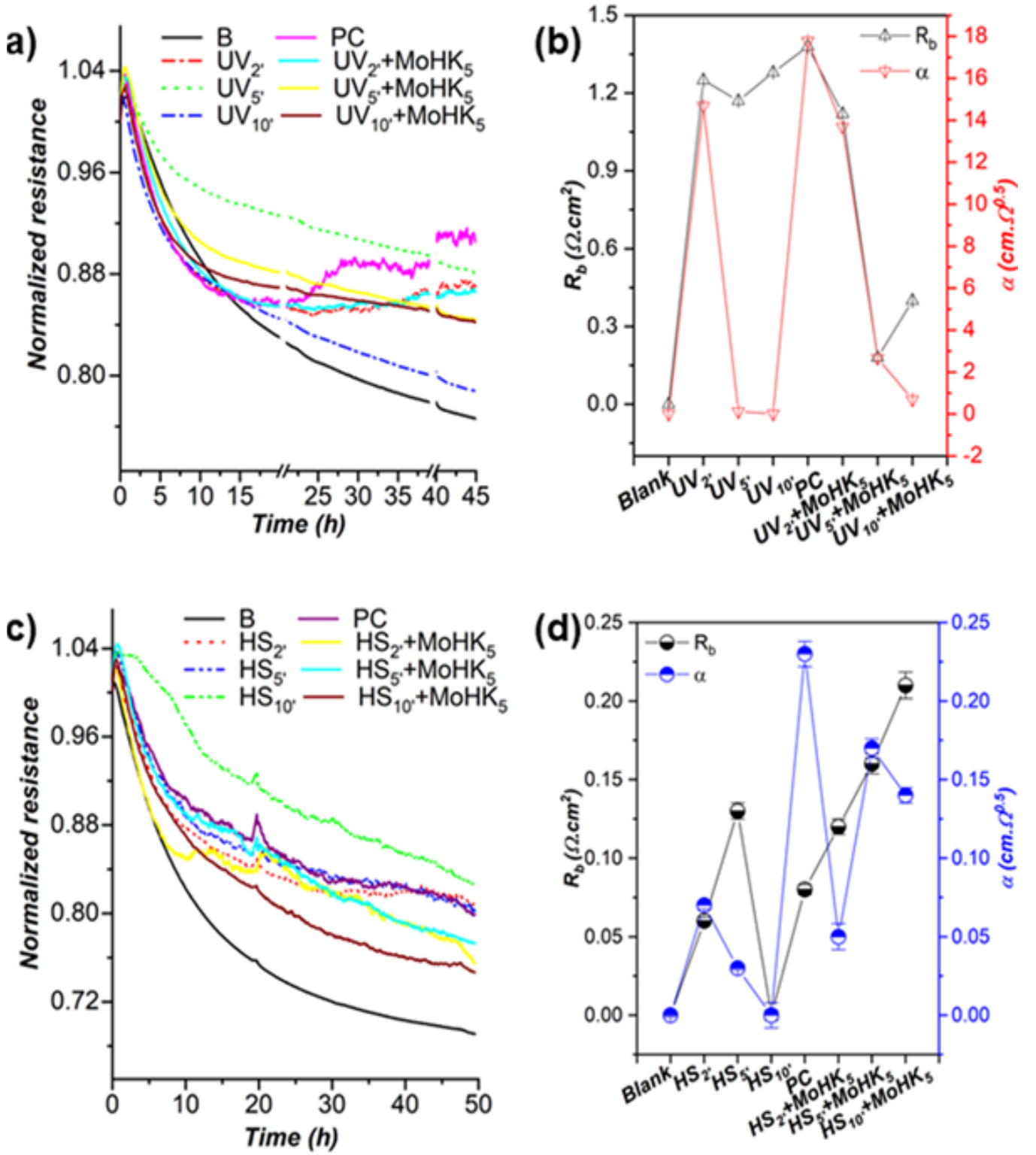


Figure 3. (a) ECIS data for RAW 264.7 cells treated with UV-irradiation (λ_m = 254 nm) and (b) its derived R_b and α values. (c) ECIS results for heat shock treated (45 ˚C) cells and (d) its corresponding R_b and α values.

UV rays cause a cascade of inflammatory responses, including the release of ROS, proinflammatory cytokines, and activation of the pain sensory pathway. Increased phospholipase activity may also occur due to oxygen radical-induced peroxidation of membrane lipids. The UV-C rays can trigger the generation of ROS, which further increases the concentration of proinflammatory cytokines and other mediator pathways such as EP4, EP2, PGE2-EP4, and LPS. To study this, a pre-incubated cells are exposed to UV radiation for 2 (acute), 5, and 10 (extended) min for both untreated and test sample treated cell lines, followed by real-time stress monitoring using ECIS. Cells exposed to harsh UVC light are subjected to determination of Z, R, and C to correlate the cell phase changes, serving as a metric for assessing the biophysical damage. This insight can further help in developing preventive strategies [27].

In **Fig.** 3(a), the cells inoculated with MoHK NPs are stable at the initial period compared to positive control and untreated cell lines. This strong cellular regeneration further favored the formation of an intact cell barrier. The wells covered in confluent cell layers is scanned to determine the impedance at different frequencies. Localized differences observed in the resistance measurements indicate the heterogeneity of the cell layer on the substrate. For better insights on cell barrier and micromotion, resistance/capacitance is recorded at low frequency, *i.e.,* 62.5 Hz (**Fig**. S6 (a) and (b)). Inter and intra changes in resistivity among the wells are compared to correlate the biophysical phenomena (**Fig.** S6 c). Here, 2 min UV-irradiation accelerated cell micromotion. In comparison, 5 min exposure may initiate cellular agitation observed in wells without MoHK. In the presence of MoHK, a distinct observation indicates that cells might be nourished with ROS scavenging species, tolerating the acute irradiation, and restricting the micromotion. This contrasts with the MoHK wells treated for 10 min. These observations are further supported by modeled data in **Fig**. S7, showing a decrease in R_b and an increase in α for MoHK-treated wells with no significant difference in C_m. The R_b and α value at 25 h, as shown in **Fig**. 3(b), provide insights into the effect of UV irradiation on a cell-electrode interface. During the UV treatment, the cell tight junction seems loosened but regains its morphology and ECM for MoHK NPs inoculated wells.

3.2 Heat-shock mediated ROS and effect of MoHK NPs

An optimal temperature is desired for cellular homeostasis. However, exposure to abrupt heat shock can cause cellular stress, modifying the biochemical and physical processes. Herein, the ECIS method assesses the biophysical phenomena by applying heat shock on RAW 264.7 cells. The interlinking mechanism between temperature-induced stress and changes in cellular function is studied *via* electrical impedance. **Fig.** 3(c) shows that cell vitality correlated with resistance change. Heat shock triggered cell agitation, causing migration resulting in higher impedance readings. However, MoHK NPs supported better recovery after heat shock for various times, *i.e.,* 2-, 5-, and 10-min. Cells observed to be stress-resistant as observed with low degree of impedance change. From **Fig.** S8 (a-b), 2 min heat shock-induced and MoHK NP-treated wells are comparable with positive control. The shock

resulted in cell micromotion causing an increased resistance. However, no characteristic resistance change is observed with prolonged exposure time. Additionally, from the post-shock treated well, an increased capacitance is also observed due to current permeated through ruptured cells. Untreated wells showed a linear increase in capacitance compared to a decreasing trend for MoHK-treated wells. Here, MoHK may acted as a shock absorber by scavenging ROS. Thus, protecting the cell and its ECM. Resistance deviation for the cells with heat shock is comparable to control (**Fig.** S8c). An increase in heat shock time is reflected with increased resistance. Notably, the well exposed to a 10-minute heat shock exhibited the highest resistance among the tested wells. Presumably, increased cell debris adhered to the micro-electrodes causing the high barrier resistance, evidenced by the fitted model for R_b shown in **Fig**. 2(d), derived from raw data in **Fig**. S9. This result indicates a rapid formation of cell barrier during post heat-shock for all MoHK treated wells, even superior to positive control. However, this initial rapid increase in R_b values could be attributed to increased cell-substrate adherence, which can also alter resistance. The increased cell-substrate attachment can also be due to the recovery of the cell's normal function influenced by MoHK, leading to a tighter and more stable cell barrier. Distinguishingly, for MoHK-treated wells, the α values increased linearly concerning heat-shock time. A slower rate of impedance change is observed in the other sample-treated wells, indicating less susceptibility to temperature-induced morphological distortion. Therefore, MoHK acted as a shock absorber by tolerating the heat- shock generated ROS and improving the cells' vitality. MoHK stabilized the heat shock-induced cellular oxidative stress in a time-dependent manner.

3.3 H_2O_2 generated ROS and MoHK as a scavenger

The H_2O_2 facilitates redox sensing and signaling inside the cell. H_2O_2 generation, transport, capture, and biological repercussions are well studied [28]. The high level of H_2O_2 triggers the radical initiation, expanding the oxidative pathways. A protective effect of MoHK is observed against H_2O_2-induced oxidative stress (**Fig.** 4 a). The anti-oxidant response from MoHK NPs is found to supersede natural anti-oxidants, *i.e.,* ascorbic acid (AA) and gallic acid (GA), even at the 10-fold concentration difference. After 7 h of sample inoculation, 1 mM of H_2O_2 is added at t= 29 h. A fall in cell resistance is observed, ascribed to the shrinkage of cells due to the oxidative stress affected by H_2O_2. Interestingly, MoHK-treated cells had robust cellular integrity compared to standard references. MoHK effectively supported the cells under stress conditions. Therefore, treated well's resistance is comparable with standards. MoHK has provided prolonged anti-inflammatory activity with high resistance up to t = 70 h, augmenting a similar effect to gallic acid and excelling effectiveness compared to AA.

A change in resistance with respect to frequency is represented in **Fig.** S10. It can be observed that both at low and high frequencies, the test samples treated wells exhibited higher resistance comparable to PC and blank. A reduction trend in resistance is marked by an increase in frequency in ECIS wells in the order of PC>$MoHK_5$>GA>M_5>AA>K_5>blank. Importantly, wells treated with MoHK NPs show better proliferation than standard anti-oxidant and pristine cells seeded well. **Fig.** S11 represents the wells' resistance deviation (S.D.) histogram. Notably,

the wells treated with MoHK NPs demonstrated a minimal shift in resistance response attributed to reduced cell micromotion. Further, PC wells showed a higher change in resistance response due to cell layer formation without oxidative stress. The remaining wells exhibited similar observations. Cell biophysical parameters are inferred from modeled data in **Fig.** S12 and compiled in **Fig.** 4(b). This demonstrates that MoHK-treated cells supported a tight junction development after H_2O_2 exposure, unlike other wells with no significant change. In contrast, MoHK untreated wells showed an impaired formation of cell tight junctions, evidenced by a flat curve in R_b and a decrease over α over-time.

A conventional H_2O_2 assay is performed correlating the oxidation of H_2O_2 to validate the ECIS results. The impact of test samples *viz.,* Kaempferol, MoO_3 NPs, and MoHK NPs on intracellular H_2O_2 levels is determined. **Fig**. 4(c) shows that pretreatment with MoHK NPs significantly reduced intracellular H_2O_2 compared to other studied samples, suggesting a potential H_2O_2 scavenging activity. This is further validated by observing cell status inoculated on gold-microelectrode in ECIS after H_2O_2 addition (*t* = 30 h) using an optical microscope (**Fig**. 4(d-i)).

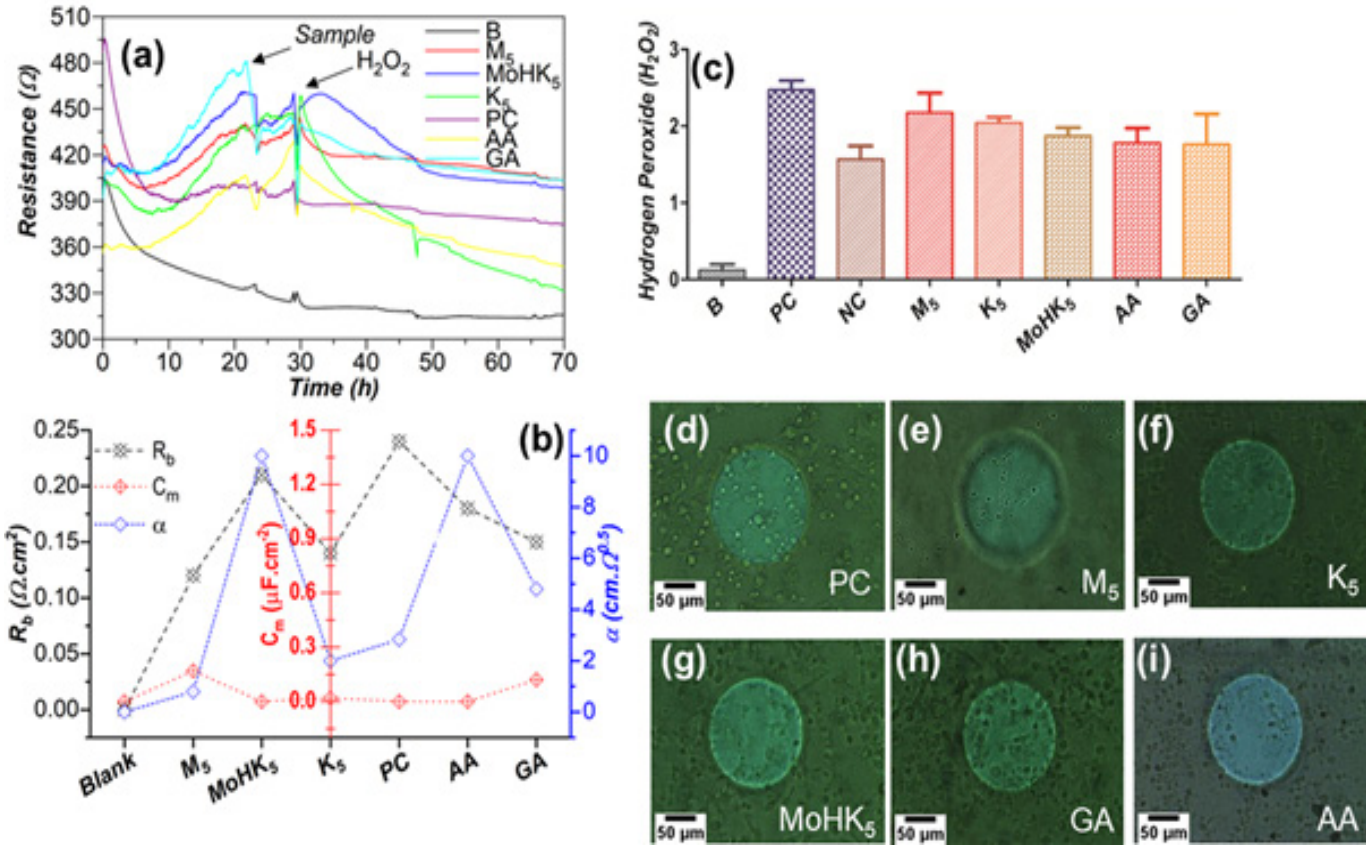


Figure 4. (a) H_2O_2-induced oxidative stress and corresponding anti-oxidant activity of the treated sample. (b) R_b α, and C_m derived from ECIS data. (c) Intracellular H_2O_2 assay with a significant difference in anti-oxidant response corresponding to test sample treatment (P<.05) determined using One-way ANOVA. (d)-(i) Optical microscopic images of gold micro-electrodes wells at 30 h (20×; scale-50 μm).

3.4 PGE2-induced cell oxidative stress and role of MoHK NPs

Inflammation is important to explore as it potentiates several diseases and disease-causing factors [29,30]. An ECIS-mediated bioimpedance investigated post-inflammation induction and subsequent anti-inflammatory activities of test samples (**Fig.** 5a). The inflammation is chemically induced using PGE2, well known as a potent pro-inflammatory cytokine activating EP4 pathway. PGE2 generation elicits inflammation and alters key cytokines such as IL-1β, IL-6, and IL-23. PGE2 also inhibits T cell receptor signaling, and proliferation leads to chronic inflammation diseases. EP4 pathway-mediated chronic inflammation is induced with lethal (10 µg) and sub-lethal (10 ng) concentrations of PGE2. The cells are inoculated with samples at t = 22 h after the grown cell is attached to the substrate. The 10 µg MoHK treated cells retain better anti-inflammatory (50% effective) against 10 µg PGE2. The µg concentration of MoHK is highly effective in controlling cellular inflammation against the ng concentration of PGE2.

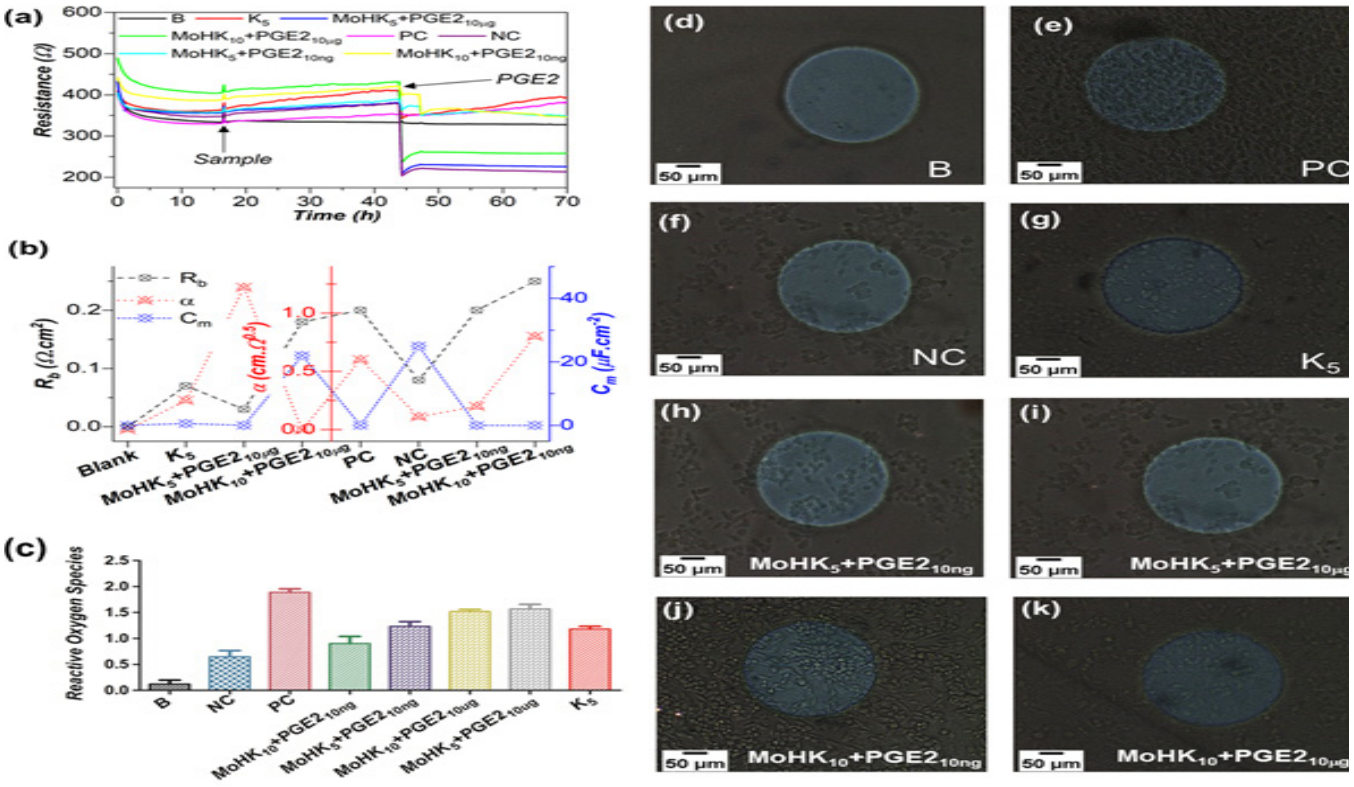


Figure 5. (a) ECIS data for effect of test sample on PGE2 induced inflammation at lethal and sub-lethal concentrations (b) Shows R_b, α, and C_m value derived from ECIS data, (c) DCFDA assay with significant difference in anti-oxidant-based anti-inflammatory response corresponding to test sample treatment (P<.001) determined using One-way ANOVA, and (d-k) Optical images of cells on gold micro-electrode in ECIS array at 60 h (20×).

In **Fig**. 4(b), the C_m measured for $MoHK_5$ treated with $PGE2_{10\mu g}$ is superior to $MoHK_{10}$ with $PGE2_{10ng}$. Likewise, calculated R_b and α shows an increasing trend with an increased concentration of MoHK for both lethal and sub-lethal doses of PGE2. This could be due to the anti-oxidant properties of nanotherapeutics under investigation *via* modulating the EP4 pathway by reducing the production of inflammatory cytokines, further inhibiting the activation of nuclear factor-kappa B (NF-κB). Our hypothesis is also supported by earlier *in vivo* studies [31]. In addition, MoHK can have a direct anti-inflammatory effect by reducing the activation of immune cells and ROS production, reducing cell necrosis. This can be observed by increased barrier resistance, promoting normal cell growth under inflammatory stress, and facilitating the formation of a cell monolayer at gold-microelectrodes by MoHK. Similarly, MoHK concentration-based resistance is also traced for a lethal dose of PGE2. However, the degree of resistance for lethal doses is lower than PC. The effectiveness of MoHK NPs in mitigating PGE2-induced oxidative stress within cells is also evaluated using the conventional DCFDA assay. In brief, RAW 264.7 cells are pretreated with Kaempferol, MoO_3, and MoHK NPs. From **Fig**. 4 (c), the test samples treated cells considerably decreased the oxidative stress than those treated with PGE2 alone. This finding indicates an anti-inflammatory potential of MoHK NPs comparable to PC. These results are further supported by the microscopic images acquired after adding PGE2 (t = 60 h) in all the wells (**Fig.** 4d-k).

ECIS's ability to electrically distinguish various biophysical cellular processes such as morphology, micromotion, adhesion, apoptosis, and proliferation in impedance signal is predominant in investigating the therapeutic potential of natural, synthetic, and semi-synthetic novel drug-like molecules. We envisage that ECIS, with attributes like non-invasiveness, real-time monitoring, and *in-situ* cell analysis, can pace up the pathology and succeeding therapeutics to understand and address the critical factors of cell damage and repairs.

4. Conclusions

The ECIS-based bioassay effectively demonstrated the dynamic cellular responses to oxidative stress and nanotherapeutics. The induction of intracellular oxidative stress has been systematically studied with RAW 264.7 cells. ECIS-derived cell behavior analyses complement conventional cytocompatibility and anti-oxidant/-inflammatory assays. The findings confirm that MoHK NPs possess significant anti-oxidant properties, as indicated by changes in cell-substrate resistance, membrane capacitance, and intercellular resistance. This study highlights the potential of ECIS as a robust tool for non-invasive pharmacological evaluation, paving the way for future research on cell-nanomaterial interactions and the development of novel therapeutic strategies.

Declaration of competing interest

The authors declare that they have no known competing financial interests.

Acknowledgments

G.P thankfully acknowledges the support of ICMR New Delhi for the award of Senior Research Fellowship (Grant no. 5/3/8/26/ITR-F2020). This

work was supported by SERB-DST, Government of India through Start-up Research Grant (SRG/2019/000238).

References

[1] S. Fulda, A.M. Gorman, O. Hori, A. Samali, Cellular stress responses: Cell survival and cell death, Int J Cell Biol 2010 (2010). https://doi.org/10.1155/2010/214074.

[2] S. Muralidharan, P. Mandrekar, Cellular stress response and innate immune signaling: integrating pathways in host defense and inflammation, J Leukoc Biol 94 (2013) 1167–1184. https://doi.org/10.1189/jlb.0313153.

[3] V. Calabrese, C. Cornelius, C. Mancuso, G. Pennisi, S. Calafato, F. Bellia, T.E. Bates, A.M. Giuffrida Stella, T. Schapira, A.T. Dinkova Kostova, E. Rizzarelli, Cellular stress response: A novel target for chemoprevention and nutritional neuroprotection in aging, neurodegenerative disorders and longevity, Neurochem Res 33 (2008) 2444–2471. https://doi.org/10.1007/s11064-008-9775-9.

[4] K. Rehman, M.S.H. Akash, Mechanism of Generation of Oxidative Stress and Pathophysiology of Type 2 Diabetes Mellitus: How Are They Interlinked?, J Cell Biochem 118 (2017) 3577–3585. https://doi.org/10.1002/jcb.26097.

[5] N. Fedoroff, Redox regulatory mechanisms in cellular stress responses, Ann Bot 98 (2006) 289–300. https://doi.org/10.1093/aob/mcl128.

[6] T. Hussain, B. Tan, Y. Yin, F. Blachier, M.C.B. Tossou, N. Rahu, Oxidative Stress and Inflammation: What Polyphenols Can Do for Us?, Oxid Med Cell Longev 2016 (2016). https://doi.org/10.1155/2016/7432797.

[7] S. Muralidharan, P. Mandrekar, Cellular stress response and innate immune signaling: integrating pathways in host defense and inflammation, J Leukoc Biol 94 (2013) 1167–1184. https://doi.org/10.1189/jlb.0313153.

[8] H.D. de Freitas Queiroz Barros, M.R. Maróstica Junior, Phenolic Compound Bioavailability Using In Vitro and In Vivo Models, in: Bioactive Compounds, Elsevier, (2019): pp. 113–126. https://doi.org/10.1016/B978-0-12-814774-0.00006-2.

[9] E.C. Dreaden, A.M. Alkilany, X. Huang, C.J. Murphy, M.A. El-Sayed, The golden age: Gold nanoparticles for biomedicine, Chem Soc Rev 41 (2012) 2740–2779. https://doi.org/10.1039/c1cs15237h.

[10] S. Mitragotri, J. Lahann, Physical approaches to biomaterial design, Nat Mater 8 (2009) 15–23. https://doi.org/10.1038/nmat2344.

[11] Z.Q. Wang, Y.W. Pan, J. Wu, H. Bin Qi, S. Zhu, Z.J. Gu, A bibliometric analysis of molybdenum-based nanomaterials in the biomedical field, Tungsten 6 (2024) 17–47. https://doi.org/10.1007/s42864-023-00225-1.

[12] I.A. de Castro, R.S. Datta, J.Z. Ou, A. Castellanos-Gomez, S. Sriram, T. Daeneke, K. Kalantar-zadeh, Molybdenum Oxides – From Fundamentals to Functionality, Advanced Materials 29 (2017) 1701619. https://doi.org/10.1002/ADMA.201701619.

[13] G. Schwarz, J. Schulze, F. Bittner, T. Eilers, J. Kuper, G. Bollmann, A. Nerlich, H. Brinkmann, R.R. Mendel, The Molybdenum Cofactor Biosynthetic Protein Cnx1 Complements Molybdate-Repairable Mutants, Transfers Molybdenum to the Metal Binding Pterin, and Is Associated with the Cytoskeleton, Plant Cell 12 (2000) 2455–2471. https://doi.org/10.1105/TPC.12.12.2455.

[14] G. Pandey, M. Marimuthu, P. Kanagavalli, V. Ravichandiran, K. Balamurugan, M.

Veerapandian, Chitosanylated MoO_3-ruthenium(II) nanocomposite as biocompatible probe for bioimaging and herbaceutical detection, ACS Biomater Sci Eng 5 (2019) 3606–3617. https://doi.org/10.1021/acsbiomaterials.9b00575.

[15] S. Hofer, S. Geisler, R. Lisandrelli, H.N. Ngoc, M. Ganzera, H. Schennach, D. Fuchs, J.E. Fuchs, J.M. Gostner, K. Kurz, Pharmacological targets of kaempferol within inflammatory pathways—a hint towards the central role of tryptophan metabolism, Antioxidants 9 (2020) 1–19. https://doi.org/10.3390/antiox9020180.

[16] L.Y. Tu, J. Pi, H. Jin, J.Y. Cai, S.P. Deng, Synthesis, characterization and anticancer activity of kaempferol-zinc(II) complex, Bioorg Med Chem Lett 26 (2016) 2730–2734. https://doi.org/10.1016/j.bmcl.2016.03.091.

[17] M. Marimuthu, B.P. Kumar, L.M. Salomi, M. Veerapandian, K. Balamurugan, Methylene blue-fortified molybdenum trioxide nanoparticles: harnessing radical scavenging property, ACS Appl Mater Interfaces 10 (2018) 43429–43438. https://doi.org/10.1021/ACSAMI.8B15841.

[18] A.K. Yagati, S.G. Chavan, C. Baek, D. Lee, M.H. Lee, J. Min, RGO-PANI composite Au microelectrodes for sensitive ECIS analysis of human gastric (MKN-1) cancer cells, Bioelectrochemistry 150 (2023) 108347. https://doi.org/10.1016/j.bioelechem.2022.108347.

[19] J.S. Kresge, C. T., Leonowicz, M. E., Roth, W. J., Vartuli, J. C., Beck, ²»ÉøÍ¸ÐÔµÄ © 19 9 2 Nature Publishing Group, Nature 359 (1992) 710–713.

[20] M. Marimuthu, C. Park, S. Kim, C.S. Choi, Real-time electrical measurement of L929 cellular spontaneous and synchronous oscillation, Int J Nanomedicine 7 (2012) 83–93. https://doi.org/10.2147/ijn.s28465.

[21] C. Lo, C.R. Keese, I. Giaever, Impedance Analysis of MDCK Cells Measured by Electric Cell-Substrate Impedance Sensing, Biophys J 69 (1995) 2800–2807. https://doi.org/10.1016/S0006-3495(95)80153-0.

[22] J. Hong, K. Kandasamy, M. Marimuthu, C.S. Choi, S. Kim, Electrical cell-substrate impedance sensing as a non-invasive tool for cancer cell study, Analyst 136 (2011) 237–245. https://doi.org/10.1039/c0an00560f.

[23] M.R. Pennington, G.R. Van de Walle, Electric Cell-Substrate Impedance Sensing To Monitor Viral Growth and Study Cellular Responses to Infection with Alphaherpesviruses in Real Time, MSphere 2 (2017) 1–12. https://doi.org/10.1128/msphere.00039-17.

[24] G.R. Pandey, P. Kanagavalli, K. Karnam, K. Thanigai Arul, P. Monisha, C.L. Dong, J.L. Chen, M. Veerapandian, J. Nirmal, Molybdenum trioxide hybridized kaempferol: double-powered nanosystem for salvaging oxidative stress and electrochemical immunoprobing of interleukin-6, Mater Today Chem 24 (2022) 100809. https://doi.org/10.1016/j.mtchem.2022.100809.

[25] O.I. Aruoma, A. Murcia, J. Butler, B. Halliwell, Evaluation of the Antioxidant and Prooxidant Actions of Gallic Acid and Its Derivatives, J Agric Food Chem 41 (1993) 1880–1885. https://doi.org/10.1021/jf00035a014.

[26] G. Schuster, A.A. do Amaral, J. Wyzykowski, M.G.P. Valenga, N.L. Boschen, G.A.R. Maia, P.R.P. Rodrigues, A.L. Gallina, Ascorbic acid as antioxidant for soybean biodiesel, Orbital 10 (2018) 183–190. https://doi.org/10.17807/orbital.v10i3.1097.

[27] L. Lisi Hruza, A.P. Pentland, Mechanisms of UV-induced inflammation, Journal of Investigative Dermatology 100 (1993) S35–S41. https://doi.org/10.1038/jid.1993.21.

[28] H. Sies, Hydrogen peroxide as a central redox signaling molecule in physiological oxidative

stress: Oxidative eustress, Redox Biol 11 (2017) 613–619. https://doi.org/10.1016/j.redox.2016.12.035.

[29] P. Hunter, The inflammation theory of disease. the growing realization that chronic inflammation is crucial in many diseases opens new avenues for treatment, EMBO Rep 13 (2012) 968–970. https://doi.org/10.1038/embor.2012.142.

[30] D. Furman, J. Campisi, E. Verdin, P. Carrera-Bastos, S. Targ, C. Franceschi, L. Ferrucci, D.W. Gilroy, A. Fasano, G.W. Miller, A.H. Miller, A. Mantovani, C.M. Weyand, N. Barzilai, J.J. Goronzy, T.A. Rando, R.B. Effros, A. Lucia, N. Kleinstreuer, G.M. Slavich, Chronic inflammation in the etiology of disease across the life span, Nat Med 25 (2019) 1822–1832. https://doi.org/10.1038/s41591-019-0675-0.

[31] M. He, T. Ichinose, S. Yoshida, T. Ito, C. He, Y. Yoshida, K. Arashidani, H. Takano, G. Sun, T. Shibamoto, PM2.5-induced lung inflammation in mice: Differences of inflammatory response in macrophages and type II alveolar cells, Journal of Applied Toxicology 37 (2017) 1203–1218. https://doi.org/10.1002/jat.3482.